

Quantum Transports in Two-Dimensions with Long Range Hopping: Shielding, Localization and the Extended Isolated State

Si-Si Wang,^{1,2,3} Kangkang Li,⁴ Yi-Ming Dai,¹ Hui-Hui Wang,^{1,3} Yi-Cai Zhang,¹ and Yan-Yang Zhang^{1,3,2,*}

¹*School of Physics and Materials Science, Guangzhou University, 510006 Guangzhou, China*

²*School of Mathematics and Information Science,
Guangzhou University, 510006 Guangzhou, China*

³*Huangpu Research and Graduate School of Guangzhou University, 510700 Guangzhou, China*

⁴*Department of Physics, Zhejiang Normal University, Jinhua 321004, China*

(Dated: August 16, 2022)

We investigate the effects of disorder and shielding on quantum transports in a two dimensional system with all-to-all long range hopping. In the weak disorder, cooperative shielding manifests itself as perfect conducting channels identical to those in the short range model, as if the long range hopping does not exist. With increasing disorder, the average and fluctuation of conductance are larger than those in the short range model, since the shielding is effectively broken and therefore long range hopping starts to take effect. Nevertheless, size scaling shows no evidence of delocalized states in the band in spite of a better connectivity from long range hopping. The all-to-all coupling expels one isolated but extended state far out of the band, whose transport is extremely robust against disorder due to absence of backscattering. The bond current picture of this isolated state shows a quantum version of short circuit through long hopping.

I. INTRODUCTION

Long range orders and behaviors from short range coupling are among the most important themes of condensed matter physics. Even theoretical models based on nearest neighbor hopping and interaction can be used to describe vast amounts of physical phenomena, including the energy band, magnetism, metal-insulator transition and topological states, etc.[1–5]. On the other hand, systems with long range coupling have attracted many interests recently. For example, in the photonic lattice, controllable long range coupling can be realized by shaping the spectrum of the optical pump[6], or by the optical gain[7]. Simulating long range hopping is proposed by periodically driven superconducting qubits[8]. Rydberg atomic lattices are considered as a promising platform for quantum information application[9], where the ultra-long coupling between atoms plays a crucial role[10–13].

Another type of long range coupling is realized by the mediation of phonons[14, 15], photons[16, 17] or an optical cavity[18–20] in different types of physical systems. The cavity induced long range coupling can even be realized in conventional electronic systems[21–23].

Theoretical studies on one-dimensional (1D) systems with long range coupling have shown many novel properties, for example, breaking of ergodicity[24], cooperative shielding in many-body systems[25], and subdiffusive phases in an open clean system[26]. The measurement-induced phase transitions of long range coupling systems are theoretically investigated[27–30], with practical applications in qubits. Based on a model with all-to-all and distance-independent hopping[31], some interesting phenomena in 1D have been predicted recently[32–34]. The first one is a cooperative shielding in the single particle picture, i.e., absence of effects from the long range hop-

ping for most of the states in the clean limit[32]. The second is the disorder-enhanced and disorder-independent transport, if a large-bias current is considered[33].

Based on state-of-the-art technologies, two-dimensional (2D) systems with long range interactions can be fabricated and studied[9, 13]. In this manuscript, we generalize the above all-to-all model to a 2D version, and investigate the quantum transports by using numerical simulations. By presenting transport evidences, we find that the cooperative shielding persists in the weak disorder limit. Although a fixed boundary condition breaks the perfect shielding, this breaking will be negligible for a sufficiently large sample. With increasing disorder, the shielding is destroyed and the transports will be remarkably different from the short range counterpart. We reveal the microscopic pictures of these transports by showing the real space distributions of bond currents, so that the roles of bonds with different lengths can be seen vividly. Furthermore the localization property is discussed by size scaling.

A unique feature of this model is the existence of a single isolated state far away from the band states[31, 32], with a large gap proportional to the size of the sample. We find it is an extended isolated state with very robust transport. The physical origins are also discussed.

This paper is organized as follows. In Section II, we introduce the tight binding model and the numerical methods we will use. The transports of the band states and the extended isolated state will be presented in Sections III and IV respectively. A brief summary is provided in Section V.

II. MODEL AND METHOD

Our 2D model is a generalization from the 1D counterpart[32, 33]. It is defined on a square lattice with the spinless Hamiltonian

$$H_{\text{LR}} = H_{\text{NN}} + H_{\text{AA}} \equiv \sum_{\langle ij \rangle} t c_i^\dagger c_j + \sum_{ij} \gamma c_i^\dagger c_j \quad (1)$$

where c_i^\dagger (c_i) creates (annihilates) an electron at site i . Here H_{NN} contains the conventional nearest neighbor hopping with the magnitude t . The second term, H_{AA} includes all-to-all and distance independent long range hopping γ , which can be realized by a cavity-assisted technology[18, 19, 33]. Throughout this paper, $t = 1$ will be used as the energy unit, and $\gamma = 1/2$ is similar to previous 1D counterparts[32, 33]. For simplicity, we adopt the sign convention that $t, \gamma > 0$. In H_{AA} , the diagonal terms $\gamma c_i^\dagger c_i$ are intentionally included. This global and trivial energy shift makes the band center of H_{LR} (referred as the ‘‘long range model’’ hereafter) be identical to that of H_{NN} (referred as the ‘‘short range model’’ hereafter), which will be convenient in following calculations.

For a finite sample with $N \equiv N_x \times N_y$ lattice sites, and with periodic boundary condition for H_{NN} in both directions (there is no difference of boundary conditions for H_{AA}), it can be easily verified that two terms of H_{LR} are commutable and therefore,

$$C_H \equiv [H_{\text{NN}}, H_{\text{LR}}] = 0. \quad (2)$$

As a result, H_{LR} and H_{NN} have common eigenfunctions[32]. Furthermore, also similar to the 1D case[32], the eigenvalues of the long range model H_{LR} are identical to those of the short range model H_{NN} , i.e.,

$$E_n^{\text{LR}} = E_n^{\text{NN}}, \quad 1 \leq n \leq N - 1, \quad (3)$$

except the highest one (the lowest one if $\gamma < 0$), which is

$$E_N^{\text{LR}} = 4t + N_x N_y \gamma \quad (4)$$

for H_{LR} . Here and throughout this manuscript, we always index eigenstates of a Hamiltonian in the ascending order of eigenvalues. Notice that E_N^{LR} is size dependent and this single state is isolated from the energy band consisting of the rest $N - 1$ eigenstates. Thus it will be called the isolated state. We can define the subspace S_N as the one spanned by this isolated state $|\psi_N\rangle$, and the subspace S_{N-1} as the one spanned by the rest $N - 1$ eigenstates $|\psi_i\rangle$. Due to the large gap $\sim N_x N_y \gamma$, these two subspaces are barely mixed when the sample size is sufficiently large and/or the disorder strength is not strong[32]. These novel mathematical structures lead to some interesting consequences. For example, because of

the above mentioned commutability, the dynamics within S_{N-1} is shielded from long-range hopping, namely it behaves as if long-range hopping does not exist. This is the cooperative shielding, a counterintuitive phenomenon found in the 1D counterpart[32]. In the following, we will see that this cooperative shielding is also manifested in 2D quantum transports.

One of our focus is disorder, which is simply included by adding a random onsite potential as

$$V = \sum_i W \cdot U_i c_i^\dagger c_i, \quad (5)$$

where U_i are independent random numbers uniformly distributed in $(-1/2, 1/2)$ and W is the single parameter to characterize the disorder strength. With nonzero W , the short range part $H_{\text{NN}} + V$ will not commute with the all-to-all part H_{AA} again. The shielding and corresponding transport phenomena will be one of the primary themes of this work.

Now let us briefly describe the main methods of calculation. At zero temperature, the two-terminal conductance G of a finite sample is proportional to the transmission (Landauer formula)[35], and can be expressed by Green’s functions as[36, 37]

$$G = \frac{e^2}{h} \text{Tr} [\Gamma_L G^r \Gamma_R G^a], \quad (6)$$

where $G^{r/a}(E) \equiv (E \pm -H - \Sigma_L^{r/a} - \Sigma_R^{r/a})^{-1}$ is the dressed retarded/advanced Green’s function of the central sample, and $\Gamma_{L(R)} = i(\Sigma_{L(R)}^r - \Sigma_{L(R)}^a)$ with $\Sigma_{L(R)}^{r/a}$ being retarded/advanced self energies due to the left (right) lead, respectively (The spin degeneracy factor 2 is omitted in this manuscript). In our calculations, we take both leads to be semi-infinite square lattices with only the nearest hopping Hamiltonian H_{NN} , since otherwise, it is numerically inaccessible to calculate the self energy of a semi-infinite lattice with long range hopping.

The local current from site i to j along the bond is[37, 38]

$$J_{i \rightarrow j} = \frac{2e^2}{h} \text{Im} [H_{ij} G_{ji}^n] (V_L - V_R), \quad (7)$$

where H_{ij} the matrix element of the bare Hamiltonian, and $G^n = G^r \Gamma_L G^a$ is the correlation function. Since it is defined in the linear response regime, we simply take the voltage difference $V_L - V_R$ between the left (source) and right (drain) leads to be unity. In this case, the net current through any transverse cross section of the sample is numerically equal to the conductance calculated from Eq. (6). Notice that all Green’s functions and self energies appearing in Eqs. (6) and (7) are energy dependent. In Sections III and IV, we will describe how we choose these energies respectively, in order to highlight

the dominating physics.

III. THE BAND

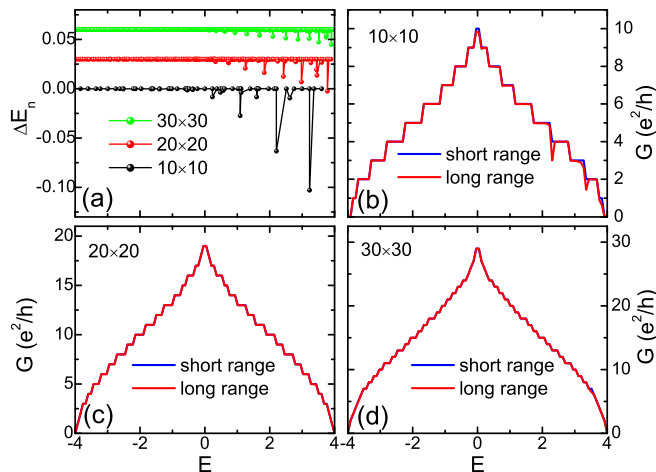


FIG. 1. (Color online) Results for zero disorder and fixed boundary condition. (a) Difference of eigenenergies $\Delta E_n \equiv E_n^{\text{LR}} - E_n^{\text{NN}}$ between the long range and short range models, for a finite sample with sizes 10×10 (black), 20×20 (red) and 30×30 (green) respectively. The latter two curves are shifted vertically for visual clarity. (b)-(d): the two-terminal conductance G as a function of Fermi energy E , for a short range (blue curve) and long range model (red curve), with sample size 10×10 (b), 20×20 (c) and 30×30 (d). The leads consists of the short range model with the same width.

In the following calculations, all samples are square shaped with the size $N_x \times N_x$ to exhibit the 2D nature. Meanwhile, fixed (hard-wall) boundary condition for the H_{NN} term (there is no boundary effects for the H_{LR} term), which is more physically realistic, especially when the sample is connected to leads. In this case, the commutator matrix C_H will not be identically zero. However, nonzero elements only occur when they are associated with boundary bonds of H_{NN} , which only constitute an extremely small portion of the matrix C_H . To check the shielding effect here, we first check the validity of Eq. (3) for isolated samples without being attached to any leads. In Fig. 1 (a), we plot the difference of eigenvalues from the long range and short range models, without disorder and in the presence of fixed boundary condition, for three different sample sizes. Notice the latter two curves are shifted vertically for better visual clarity. One can see that remarkable differences mostly occur in the high energy region near the band top (and also near the isolated state), and the difference shrinks with increasing sample size. Therefore it is reasonable to expect the shielding effect recovers for sufficiently large sample.

As an example of physical observable, the two-terminal conductance G of a sample connected with leads will be

calculated by using Eq. (6). Notice that all Green's functions and self energies appearing in Eq. (6) are energy dependent. Here, we adopt a uniform energy E among the central sample and leads, i.e., $G(E) = \frac{e^2}{h} \text{Tr} [\Gamma_L(E)G^r(E)\Gamma_R(E)G^a(E)]$, so that wavefunctions in these regions can have a best mode match, which is expected from the cooperative shielding.

The resulting G of the long range model as a function of Fermi energy E is presented as red curves in Fig. 1 (b)-(d), for different sample sizes. For comparison, the result for the short range model with the same size is also plotted as blue curves in each panel. It is interesting to see that these two types of results match excellently, exhibiting typical quantization steps of perfect transmissions. These almost perfectly quantized transmissions imply that there is almost no scattering in the sample or at the lead-sample interfaces. Distinguishable differences only occur occasionally in the high energy region in Fig. 1 (b), i.e., the smallest sample. In other words, the electron from the left lead (made up of a short range model) can transmit through the long range model sample with negligible backscattering, just as what happens in a ballistic short range model sample. These results reflect the cooperative shielding in 2D quantum transport, when disorder is absent.

We have seen that in the clean limit, the quantum transport through the 2D long range model is identical to that in the short range model, which is a manifestation of the cooperative shielding in 2D. Now we will investigate the effect from disorder. Disorder breaks Eq. (2) and thus may also break the shielding. In Fig. 2, we present the disorder averaged conductance $\langle G \rangle$ (first row) and its standard deviation ΔG (second row) as functions of the Fermi energy E , for different disorder strengths W . When $W = 3$ [panels (a) and (e)], similar to the clean limit, the results for the short range (blue curves) and the long range (red curves) models are identical. This suggests that the shielding practically survives through weak disorder, which was also observed in 1D [32].

With increasing disorder, for example, $W = 5$ [Fig. 2 (b) and (f)], the results for short and long range models start to deviate gradually. In the case of strong disorder, $W = 7, 11$, both the conductance and its fluctuation of the long range model are remarkably larger than those of the short range counterpart. In these situations, the cooperative shielding is destroyed. The existence of long range hopping gives rise to better transport (i.e., larger conductance) in the strong disorder limit.

In order to have a microscopic understanding of these quantum transports, for example, contributions from short and long range hoppings, we present distributions of bond currents associated with some typical regimes in Fig. 3. Due to the all-to-all nature of the hopping, there are too many ($\sim (N_x N_y)^2$) bonds with varying lengths intersecting each other, and densely distributed on the lattice. This makes it difficult to present a full and dis-

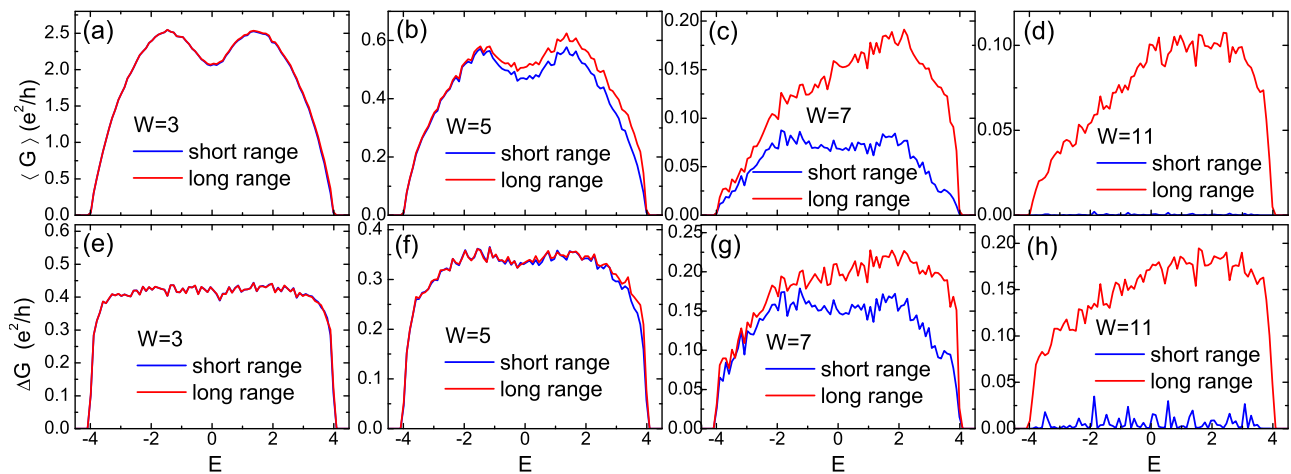


FIG. 2. (Color online) The disorder averaged conductance $\langle G \rangle$ (first row) and its standard deviation ΔG (second row) as functions of Fermi energy E , for different disorder strengths W as shown. The blue (red) curve is for the short (long) range model. The sample size is 40×40 and each data point is an average over 1000 disorder samples. All energies are in units of t .

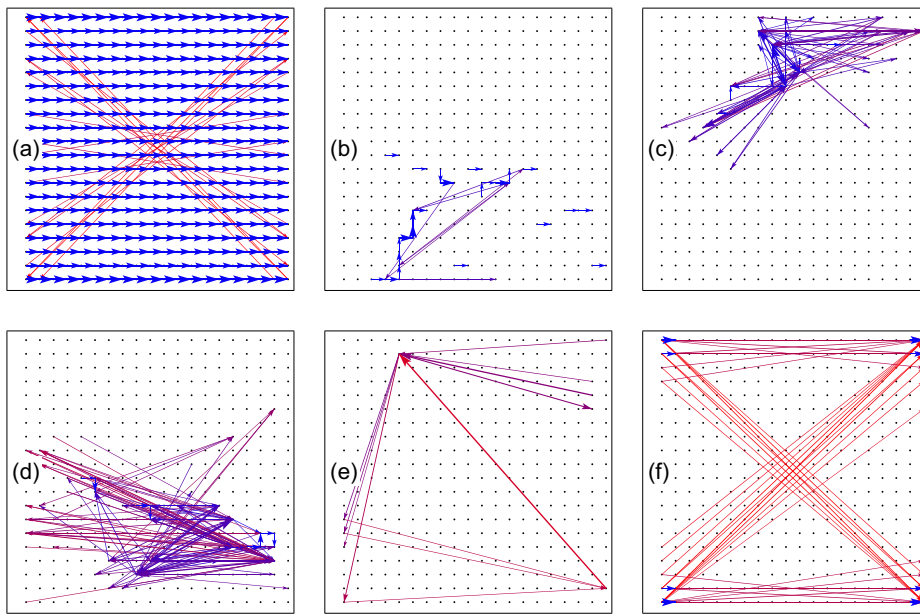


FIG. 3. (Color online) Distribution of bond currents for a certain disorder configuration on a 20×20 lattice, with the source (drain) lead connected to the left (right) boundary. (a)-(e): Fermi energy $E = 1$ in the band, with disorder strength $W = 0, 3, 5, 7, 11$, respectively. (f): Sample Fermi energy $E = 203.71$ at the EIS, with $W = 7$, discussed in Section IV. Each arrow connecting two sites represents the corresponding bond (thus its length indicating the bond length), with the size of the *arrowhead* alone to indicate the magnitude of its current. For visual clarity, only currents with $J \geq 0.4J_{\max}$ are displayed, and long (short) bonds are plotted in red (blue) color, while intermediately long bonds in purple color.

tinguishable picture of *all* bond currents, as in conventional short range models[38]. Therefore for the purpose of displaying the dominating physics clearly, we adopt some technical tactics in plotting Fig. 3. Firstly, a small sample with 20×20 sites is used. This is smaller than those used in Fig. 2, but we have checked (but not shown

here) that the physics is identical. Secondly, only currents with magnitudes $J \geq 0.4J_{\max}$ are displayed, where J_{\max} is the maximum magnitude of bond current in this sample. Therefore the displayed currents do not obey the current conservation. Thirdly, the magnitude of a bond current is represented by the size of the *arrowhead* only,

while the size of the arrow shaft still represents the real size of the bond connecting two sites. For a better visual clarity, longer (shorter) bonds are plotted in red (blue) color. We do so because, besides the current flowing on it, the actual position and length of each bond are also important information.

Fig. 3 (a) is the result for zero disorder, corresponding to the case shown in Fig. 1 (c). It can be seen that now the currents are almost uniformly carried by nearest bonds (blue arrows), and contributions from most long range bonds are small. This is a clear picture of the cooperative shielding: long range coupling does not play a role as a result of a delicate quantum coherent effect. Small currents along a few long range bonds (red arrows with small arrowheads) can be attributed to resonant states between hard wall boundaries.

In the presence of weak disorder, Fig. 3 (b), the current distribution is also disordered, and contributions from long range bonds start to increase. We notice that this corresponds to the transport shown in in Fig. 2 (a) and (e), where the conductances from the short range and long range models still match well. In other words, although the transports are carried by short range and long range bonds, the total current is still very close to that of the short range model. This is another subtle manifestation of the word, the *cooperative* shielding[32]. With larger disorder, as shown in Fig. 3 (c) and (d), the currents distribute in a more chaotic pattern, with long range bonds trying to connect localization centers of the wavefunction.

With these pictures, now we can understand more about Fig. 2. When disorder is strong, the shielding is broken and therefore the electron can hop along long bonds between localization centers. Such a better connectivity and mobility gives rise to a conductance larger than that of the short range model. In short range models of localization, it was recently found that microscopically, the dominating transport path can be pinned within a certain range of model parameters (e.g., Fermi energy and disorder potential) [39], since endeavors must be made to find another continuous path composed of sequential short range bonds. However here, thanks to the all-to-all connectivity, an entirely new path can be found more easily upon change, so that the pinning effect is reduced. Therefore, the transport will be more mutable and sensitive with the change of model parameters, e.g., the disorder potential. This leads to larger fluctuations of the conductance at strong disorder displayed in Fig. 2 (g) and (h).

Now we discuss this question: will the long range hopping lead to a metallic (delocalized) state in the thermodynamic limit? To answer this, one needs to perform numerical scaling on some transport quantities. A commonly used quantity is the localization length normalized by the sample size, which can be extracted from the transfer matrix method[40, 41]. However, a transfer

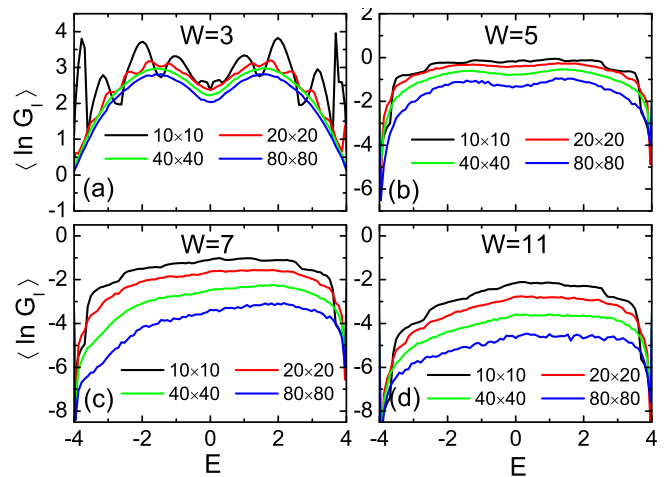


FIG. 4. (Color online) Disorder averaged $\langle \ln G_I \rangle$ as a function of Fermi energy E for different sample sizes: 10×10 (black), 20×20 (red), 40×40 (green), 80×80 (blue), at different disorder strengths: (a) $W = 3$, (b) $W = 5$, (c) $W = 7$, (d) $W = 11$. The average is over 1000 samples for the largest size and 5000 samples for other sizes.

matrix can only be applicable to a model with a very finite hopping range. Here instead, we use the numerical scaling on the intrinsic conductance G_I which is defined as[42]

$$\frac{1}{G_I} = \frac{1}{G} - \frac{1}{M_c}, \quad (8)$$

with M_c the number of active channels at Fermi energy in the lead. The second term $\frac{1}{M_c}$ is used to deduct the effect of contact resistance so that the intrinsic transport property of the sample can be manifested. This intrinsic conductance of square shaped ($N_x \times N_x$) samples can also be used to evaluate the scaling function $\beta = \frac{d(\ln G_I)}{d \ln N_x}$ of the metal-insulator transition, where $\langle \dots \rangle$ stands for averaging over the disorder ensemble [43–45]. An increase (decrease) of $\ln G_I$ with increasing $\ln N_x$ indicates a metal (insulator) phase.

In Fig. 4, the size scalings of $\langle \ln G_I \rangle$ is plotted for different disorder strengths. In the weak disorder regime shown in Fig. 4 (a), there are significant finite-size fluctuations for the smallest size (black curve). After they are smoothed out in large sizes, it is clear that $\ln G_I$ is decreasing with increasing sample size, in the whole energy region. This decreasing is more significant at larger disorder strengths, as shown in the rest panels of Fig. 4. There seem to be some curve crossings around two ends of the energy interval. We have checked that this only occurs for the smallest size 10×10 , and that for larger sizes, $\ln G_I$ is still monotonically decreasing. As a summary, all band states of this 2D long range model are localized. This is not surprising since delocalization is expected in the weak disorder region, but here the long range system

is shielded to mimic a short range one, a conventional 2D system in the orthogonal class that has no delocalized states[2, 3, 46]. In one word in this 2D model, the long range coupling does not enhance the transport in the band enough to make a really delocalized state in the presence of disorder.

IV. THE ISOLATED STATE

One should remember that there is a single state (4) isolated far away ($\sim N_x^2\gamma$) from the band investigated above. In 1D with periodic boundary condition, it was found that the wavefunction of this isolated state is fully extended with a uniform magnitude and phase among all lattice sites[32]. In 2D and in the fixed boundary condition here, we have checked (but do not show here) that this uniformity is only slightly changed, and the energy value of this state is also slightly different from that given in Eq. (4). In the presence of disorder, in order to characterize the localization property of the n -th eigenstate $\psi_{n,i}$, we use the fractal dimension of the wavefunction defined as[3, 47]

$$\Gamma_n = \frac{\ln(\text{IPR})_n}{\ln N_x}, \quad (9)$$

where $(\text{IPR})_n$ is the inverse participation ratio $(\text{IPR})_n \equiv \sum_i |\psi_{n,i}|^4$. In a 2D system, an extended state corresponds to $\Gamma_n \sim 2$ while a localized state corresponds to $\Gamma_n \ll 2$.

In Fig. 5, red symbol-curves are fractal dimensions Γ_n of four representative states as functions of disorder strength W : the band bottom (square), the band center (circle), the band top (up triangle), and the isolated state (down triangle). Panels (a) and (b) are for a 40×40 and a 80×80 sample respectively. For comparison, results from a short range model are also shown as blue symbol curves. We can see that for eigenstates in the band, Γ_n decays to zero rapidly with increasing disorder, which is consistent with above conclusion that they are localized.

On the contrary, the fractal dimension for the isolated state is robustly quantized as 2 until W approaches $\sim N_x^2\gamma$, the gap from the band. We remind that it is a *single* state instead of a flat band consisting of a continuum of *states*. Thus for an electron in this state, there is *no* other state for it to be scattered onto, and therefore any back-scattering or skew-scattering is forbidden. The robustness of this state's transport is protected by the large gap from the band, unless the impurity strength is strong enough $\sim N_x^2\gamma$ to overcome this large gap. This is the physical origin of the robust transport of this state, which we call it the extended isolated state (EIS) hereafter.

The above results are from a sample decoupling from the environment. Now we still simulate the quantum

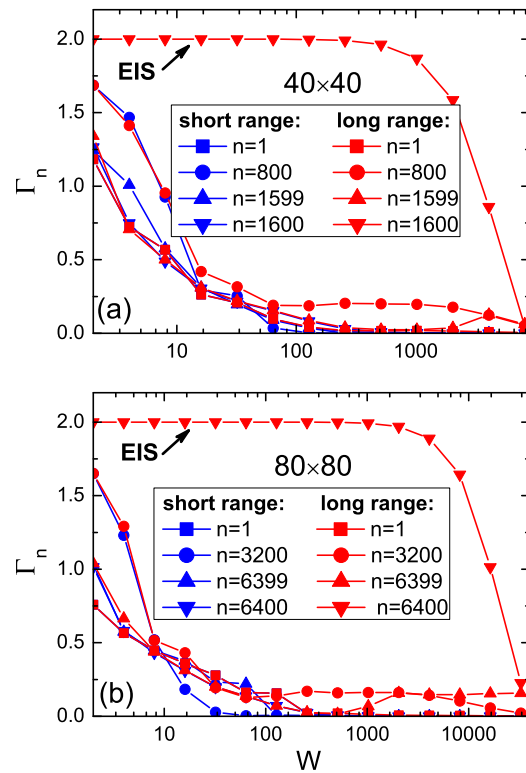


FIG. 5. (Color online) The fractal dimension Γ_n of the n -th eigenstate as a function of disorder strength W , for a certain sample with size 40×40 (a), and size 80×80 (b). Blue (red) color is for the short (long) range model. Notice horizontal scales in two panels are different.

transports of the EIS by attaching leads to both ends of the sample. Here, since the condition Eq. (2) for perfect shielding is partially destroyed by the fixed boundary condition, we have checked that this EIS is not an eigenstate of the short range model (played as leads). In other words, no state in the lead can actually match the EIS in the central sample. Therefore in this section, when calculating transports by using Eqs. (6) and (7), we simply treat the leads as electron reservoirs with a fixed Fermi energy E_L (respect to its band center) and vary the Fermi energy of the sample E around the EIS, e.g., $G(E) = \frac{e^2}{h} \text{Tr} [\Gamma_L(E_L) G^r(E) \Gamma_R(E_L) G^a(E)]$.

In Fig. 6 (a), conductances of two disorder configurations [C1 (black curve) and C2 (red curve)] as functions of E are presented as solid curves, with size 40×40 and disorder strength $W = 16$. The corresponding density of states (DOS)

$$\rho(E) = -\frac{1}{\pi N_x^2} \text{Im} G^r(E), \quad (10)$$

are also plotted as dots. Due to the coupling with leads, both the conductance and DOS profiles are broadened as smooth peaks. The first obvious observation is the

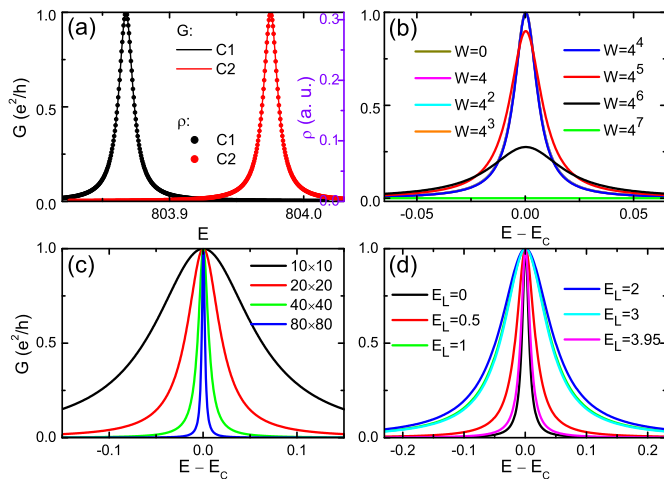


FIG. 6. (Color online) Two-terminal conductance G as a function of the Fermi energy in the sample, for the extended isolated state. (a) For two disorder configurations, C1 (black curve) and C2 (red curve). The corresponding DOS ρ (referenced to the right axis) are also plotted as dots. (b) For different disorder strengths W . (c) For different sample sizes. (d) With different energies E_L in leads. If not otherwise stated in the panel, parameters are as follows: $W = 16$, $E_L = 0$ and size 40×40 . In panels (b), (c) and (d), all curves have been horizontally shifted to the same peak center.

perfect coincidence between profiles of $G(E)$ and $\rho(E)$, after appropriate scaling in the vertical direction. This can be understood as follows. The zero-temperature conductance of a 2D crystal can also be expressed in the Thouless form [42, 48],

$$G = \pi \rho(E) \left. \frac{\partial^2 E}{\partial k_x^2} \right|_{k_x=0}, \quad (11)$$

where k_x is the wavevector along the transport direction. Notice the last factor $\frac{\partial^2 E}{\partial k_x^2}$ is a curvature of the band $E(\mathbf{k})$. However here, there is only a single state for which no curvature can be defined, so this factor plays no role and thus has no energy dependence. As a result for a concrete sample, the energy dependence of the conductance is simply proportional to that of the DOS, both with the same spectrum width determined by the imaginary part of the N -th eigenvalue of the dressed (non-Hermitian) Hamiltonian $H + \Sigma_L + \Sigma_R$.

The second observation from Fig. 6 (a) is more important. The peak value of the conductance is always quantized as unity, which means the EIS carries a perfectly conducting channel. This reflects the absence of backscattering for the EIS, as predicted from Fig. 5 above. Conductance peaks with other W are shown in Fig. 6 (b). The robust transport of EIS persists at least to $W = 4^4 = 256$ for the sample size 40×40 , consistent with Fig. 5 (a). To reveal the microscopic origin of this robust transport, we again turn to the real space

distribution of bond currents at the conductance peak, for a smaller sample as shown in Fig. 3 (f). The picture is simple and clear: the dominating currents are flowing through very long bonds connecting the left and right boundaries *directly*. This configuration helps the electron to circumvent any impurities in the sample bulk, leading to a remarkably robust transport independent of disorder. We thus call it a quantum short circuit effect.

The size dependence of the conductance peak is presented in Fig. 6 (c), where larger samples result in sharper conductance peaks. This is not surprising because a larger size leads to a finer resolution of energy and thus a smaller broadening. Fig. 6 (d) are conductance peaks with different lead energies E_L (respect to its band center). It is interesting to notice that sharpest peaks correspond to injecting electrons from the band edge ($E = 3.95$) or the band center ($E \sim 0$) of the leads. These two cases correspond to the low DOS and the van Hove singularity[49] respectively.

V. SUMMARY

We numerically investigate the quantum transports of a 2D system with long range hopping. In the band, the transport is almost identical to that in the corresponding short range system for a large sample size and weak disorder, as a manifestation of the cooperative shielding. This shielding is broken at strong disorder, and the average and fluctuation of the conductance are larger than those in the short range mode. These can be understood as a better connectivity and the destruction of path pinning from long range coupling. From size scaling of the intrinsic conductance, no evidence of delocalization is found for the band states. As for the isolated state, its transport of a unit conducting channel is highly robust against disorder, which can be depicted as an extended state protected by the large gap from scattering, or a quantum short circuit effect in the real space.

ACKNOWLEDGEMENTS

This work was supported by National Natural Science Foundation of China under Grant Nos. 12104108, 11774336 and 11874127, the Joint Fund with Guangzhou Municipality under Nos. 202201020198 and 202201020137, and the Starting Research Fund from Guangzhou University under Grant Nos. RQ2020082, RQ 2020083 and 62104360.

* yanyang@gzhu.edu.cn

[1] G. D. Mahan, *Condensed Matter in a Nutshell*, (Princeton University Press, Princeton and Oxford, 2011).

- [2] P. A. Lee and T. V. Ramakrishnan, *Rev. Mod. Phys.* **57**, 287 (1985).
- [3] F. Evers and A. D. Mirlin, *Rev. Mod. Phys.* **80**, 1355 (2008).
- [4] M. Z. Hasan and C. L. Kane, *Rev. Mod. Phys.* **82**, 3045 (2010).
- [5] X.-L. Qi and S.-C. Zhang, *Rev. Mod. Phys.* **83**, 1057 (2011).
- [6] B. A. Bell, K. Wang, A. S. Solntsev, D. N. Neshev, A. A. Sukhorukov, and B. J. Eggleton, *Optica* **4**, 1433 (2017).
- [7] Y. G. N. Liu, P. S. Jung, M. Parto, D. N. Christodoulides, and M. Khajavikhan, *Nat. Phys.* **17**, 704 (2021).
- [8] M. M. Roses, H. Landa, and E. G. Dalla Torre, *Phys. Rev. Res.* **3**, 033288 (2021).
- [9] I. Cong, H. Levine, A. Keesling, D. Bluvstein, S.-T. Wang, and M. D. Lukin, *Phys. Rev. X* **12**, 021049 (2022).
- [10] C. H. Greene, A. S. Dickinson, and H. R. Sadeghpour, *Phys. Rev. Lett.* **85**, 2458 (2000).
- [11] C. Boisseau, I. Simbotin, and R. Côté, *Phys. Rev. Lett.* **88**, 133004 (2002).
- [12] V. Bendkowsky, B. Butscher, J. Nipper, J. P. Shaffer, R. Löw, and T. Pfau, *Nature (London)* **458**, 1005 (2009).
- [13] D. Bluvstein, H. Levine, G. Semeghini, T. T. Wang, S. Ebadi, M. Kalinowski, A. Keesling, N. Maskara, H. Pichler, M. Greiner, V. Vuletić, and M. D. Lukin, *Nature (London)* **604**, 451 (2022).
- [14] P. Jurcevic, B. P. Lanyon, P. Hauke, C. Hempel, P. Zoller, R. Blatt, and C. F. Roos, *Nature (London)* **511**, 202 (2014).
- [15] E. Akkermans, A. Gero, and R. Kaiser, *Phys. Rev. Lett.* **101**, 103602 (2008).
- [16] J. Grad, G. Hernandez, and S. Mukamel, *Phys. Rev. A* **37**, 3835 (1988).
- [17] G. L. Celardo, F. Borgonovi, M. Merkli, V. I. Tsifrinovich, and G. P. Berman, *J. Phys. Chem. C* **116**, 22105 (2012).
- [18] E. Orgiu, J. George, J. Hutchison, E. Devaux, J. Dayen, B. Doudin, F. Stellacci, C. Genet, J. Schachenmayer, C. Genes, G. Pupillo, P. Samorì, and T. W. Ebbesen, *Nat. Mater.* **14**, 1123 (2015).
- [19] J. Schachenmayer, C. Genes, E. Tignone, and G. Pupillo, *Phys. Rev. Lett.* **114**, 196403 (2015).
- [20] J. Feist and F. J. Garcia-Vidal, *Phys. Rev. Lett.* **114**, 196402 (2015).
- [21] E. Orgiu, J. George, J. A. Hutchison, E. Devaux, J. F. Dayen, B. Doudin, F. Stellacci, C. Genet, J. Schachenmayer, C. Genes, G. Pupillo, P. Samorì, and T. W. Ebbesen, *Nature Mater.* **14**, 1123 (2015).
- [22] G. L. Paravicini-Bagliani, F. Appugliese, E. Richter, F. Valmorra, J. Keller, M. Beck, N. Bartolo, C. Rössler, T. Ihn, K. Ensslin, C. Ciuti, G. Scalari, and J. Faist, *Nat. Phys.* **15**, 186 (2018).
- [23] C. Ciuti, *Phys. Rev. B* **104**, 155307 (2021).
- [24] D. Mukamel, S. Ruffo, and N. Schreiber, *Phys. Rev. Lett.* **95**, 240604 (2005).
- [25] L. F. Santos, F. Borgonovi, and G. L. Celardo, *Phys. Rev. Lett.* **116**, 250402 (2016).
- [26] A. Purkayastha, M. Saha, and B. K. Agarwalla, *Phys. Rev. Lett.* **127**, 240601 (2021).
- [27] T. Minato, K. Sugimoto, T. Kuwahara, and K. Saito, *Phys. Rev. Lett.* **128**, 010603 (2022).
- [28] M. Block, Y. Bao, S. Choi, E. Altman, and N. Y. Yao, *Phys. Rev. Lett.* **128**, 010604 (2022).
- [29] T. Müller, S. Diehl, and M. Buchhold, *Phys. Rev. Lett.* **128**, 010605 (2022).
- [30] S. Xu, *Physics* **15**, 2 (2022).
- [31] F. M. Cucchietti and H. M. Pastawski, *Physica A* **283**, 302 (2000).
- [32] G. L. Celardo, R. Kaiser, and F. Borgonovi, *Phys. Rev. B* **94**, 144206 (2016).
- [33] N. C. Chávez, F. Mattiotti, J. A. Méndez-Bermúdez, F. Borgonovi, and G. L. Celardo, *Phys. Rev. Lett.* **126**, 153201 (2021).
- [34] Horacio M. Pastawski, *Physics* **14**, 57 (2021).
- [35] Y. Imry and R. Landauer, *Rev. Mod. Phys.* **71**, S306 (1999).
- [36] S. Datta, *Electronic Transport in Mesoscopic Systems* (Cambridge University Press, Cambridge, U.K., 1995).
- [37] S. Datta, *Quantum Transport: Atom to Transistor* (Cambridge University Press, Cambridge, U.K., 2005).
- [38] H. Jiang, L. Wang, Q.-F. Sun and X. C. Xie, *Phys. Rev. B* **80**, 165316 (2009).
- [39] G. Lemarié, *Phys. Rev. Lett.* **122**, 030401 (2019).
- [40] A. MacKinnon and B. Kramer, *Z. Phys. B* **53**, 1 (1983).
- [41] B. Kramer and A. MacKinnon, *Rep. Progr. Phys.* **56**, 1469 (1993).
- [42] D. Braun, E. Hofstetter, G. Montambaux and A. MacKinnon, *Phys. Rev. B* **55**, 7557 (1997).
- [43] K. Slevin, P. Markoš and T. Ohtsuki, *Phys. Rev. Lett.* **86**, 3594 (2001).
- [44] J. Bang and K. J. Chang, *Phys. Rev. B* **81**, 193412 (2010).
- [45] W. Chen, C. Wang, Q. Shi, Q. Li, and X. R. Wang, *Phys. Rev. B* **100**, 214201 (2019).
- [46] E. Abrahams, P. W. Anderson, D. C. Licciardello, and T. V. Ramakrishnan, *Phys. Rev. Lett.* **42**, 673 (1979).
- [47] Y. Wang, X. Xia, L. Zhang, H. Yao, S. Chen, J. You, Q. Zhou, and X.-J. Liu, *Phys. Rev. Lett.* **125**, 196604 (2020).
- [48] J. T. Edwards and D. G. Thouless, *J. Phys. C* **5**, 807 (1972).
- [49] E. N. Economou, *Green's Functions in Quantum Physics*, 3rd Edition, (Springer-Verlag Berlin Heidelberg, 2006).